Webb et al., https://doi.org/10.1083/jcb.201701084

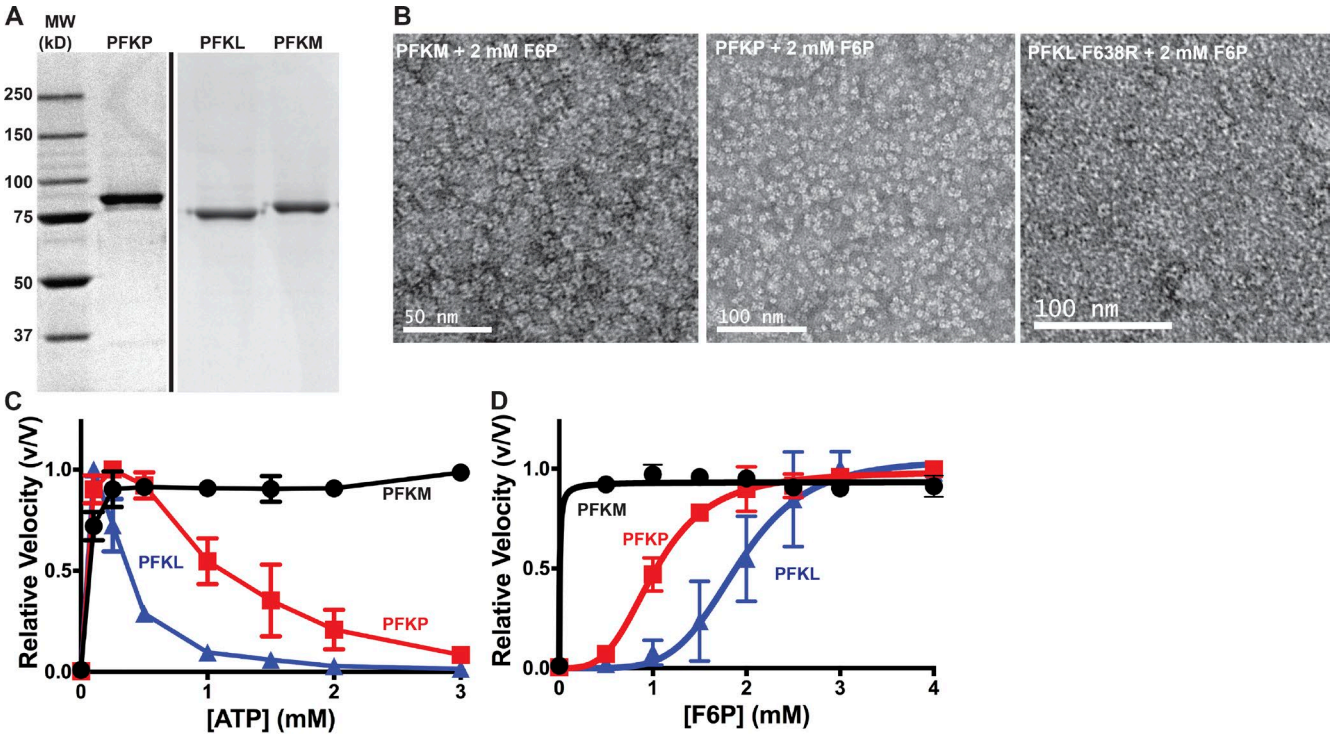

E

Comparison of kinetic parameters of wild type and chimeric PFK1. Kinetic properties of wild type and chimeric protein were determined by modeling the hyperbolic and the sigmoidal part of the curve to the Michaelis-Menten and Hill equations, respectively. V_{max}, maximum velocity of reaction in units/μg PFK1; $S_{0.5,F6P}$, substrate concentration at half-maximum activity; n_{F6P}, Hill coefficient. Measurements were carried out at pH 7.4 with 0.125 mM ATP. Means ± SEM from 3 independent measurements from two preparations of protein. ND, not determined.

Parameter	PFKL	PFKP	PFKM	CatP/RegL
V_{max}	18.0 ± 2.2	62.1 ± 1.6	61.5 ± 1.8	11.3 ± 0.5
$S_{0.5,F6P}$	2.0 ± 0.2	1.0 ± 0.1	<0.5	1.0 ± 0.1
n_{F6P}	4.9 ± 1.7	3.4 ± 0.4	ND	2.8 ± 0.5

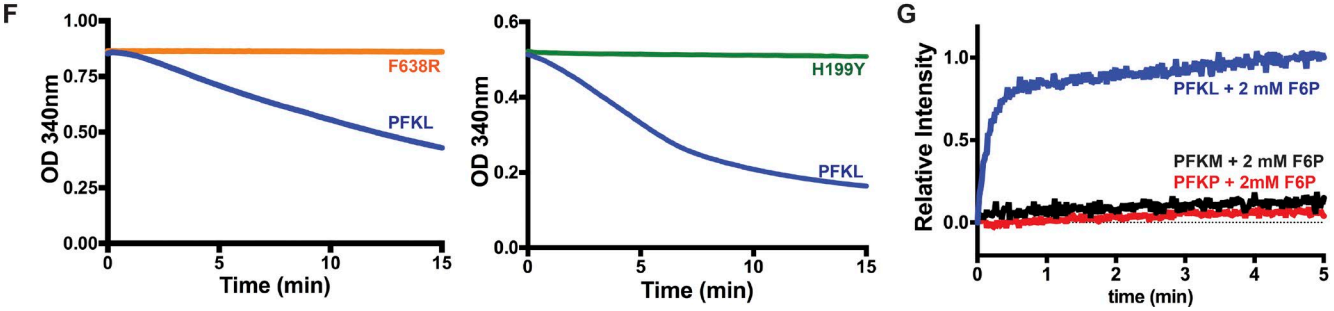

Figure S1. **Activity, TEM, and light scattering of purified recombinant wild-type and mutant PFK1.** (A) Coomassie-stained SDS-PAGE of purified PFKP, PFKL, and PFKM. (B) TEM images of PFKM, PFKP, and PFKL-F638R in buffer containing 2 mM F6P. (C and D) Allosteric regulation of PFKL (blue), PFKP (red), and PFKM (black) by ATP (C) and F6P (D). The relative velocity (v/V) is expressed as the activity of each condition (v) relative to the maximal activity of the enzyme (V) in each titration. ATP activation and inhibition was performed at pH 7.4 with 2 mM F6P, whereas F6P affinity was performed at pH 7.4 with 0.1 mM ATP. Data are means ± SD of three determinations from two separate protein preparations. (E) Table of kinetic parameters of wild-type and chimeric PFK1. (F) Absorbance at 340 nm over 15 min for wild-type (blue), F638R (orange), or H199Y (green) PFKL. PFKL activity is linked to NADH reduction and was detected as a decrease in absorbance at 340 nm. (G) 90° light scattering at the 200 μg/ml PFKL (blue), PFKP (red), and PFKM (black) upon the addition of 2 mM F6P at time 0. Data are representative of three determinations from two separate protein preparations.

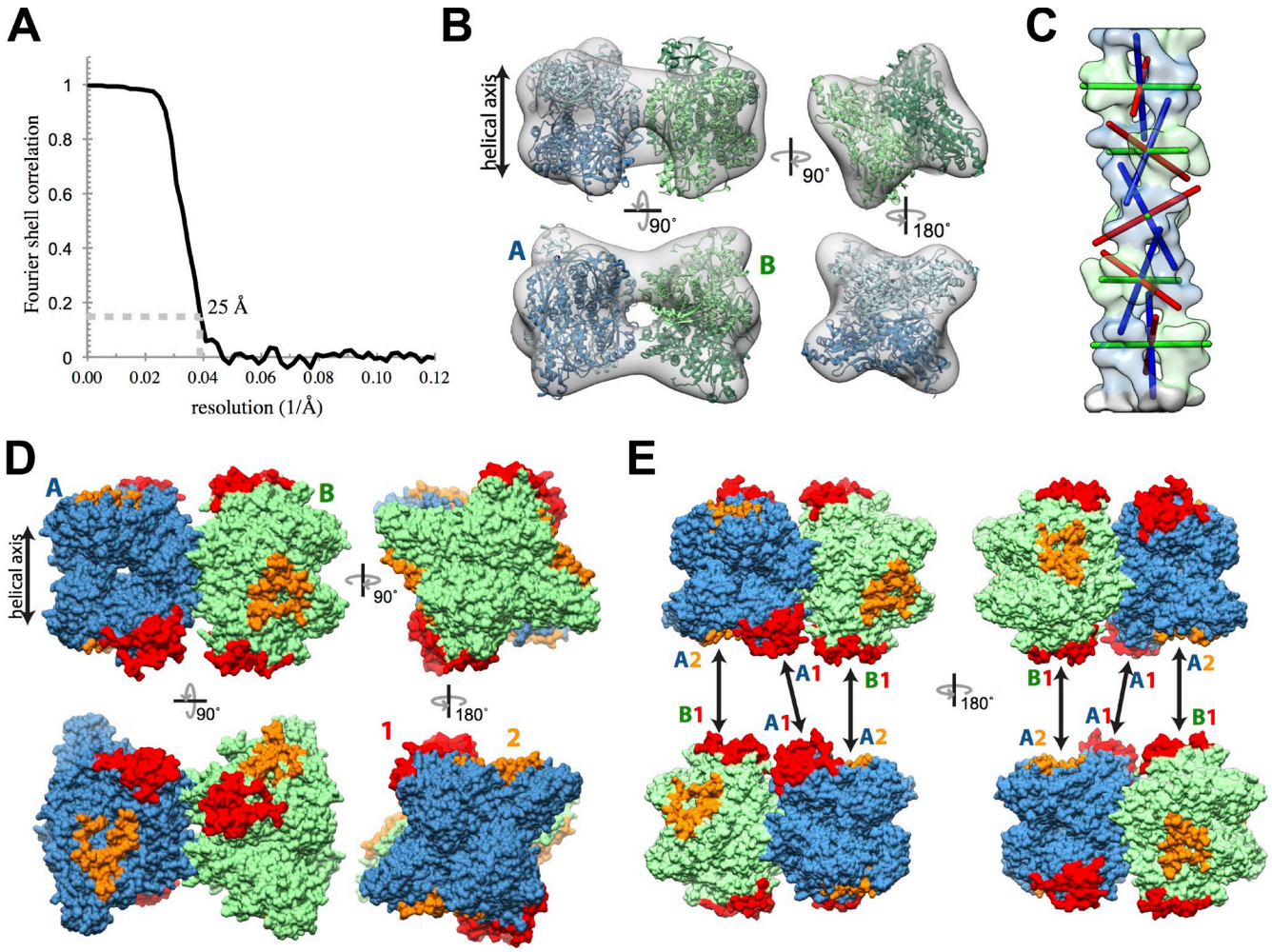

Figure S2. **Determination of the PFKL filament structure.** (A) Fourier shell correlation plot for the reconstruction of PFKL filaments indicates a resolution of 25 Å. (B) Fit of the PFKP crystal structure into EM density corresponding with the helical asymmetric unit (one tetramer). (C) Local twofold symmetry axes for each PFKL D2 tetramer are shown. The green axis is perpendicular to the helical symmetry axis and relates the two halves of each A and B dimer, resulting in an apolar filament. The red and blue axes are rotated from the vertical by ~30°, which results in the A and B dimers presenting different surfaces as assembly interfaces. (D) The two helical assembly interfaces are colored red (interface 1) and orange (interface 2) on the PFKL tetramer. (E) Diagram of intertetramer interactions that drive filament assembly. Interactions are between dimer B interface 1 (B1) and dimer A interface 2 (A2) as well as dimer A interface 1 (A1) to A1. The B2 surface is exposed in the polymer.

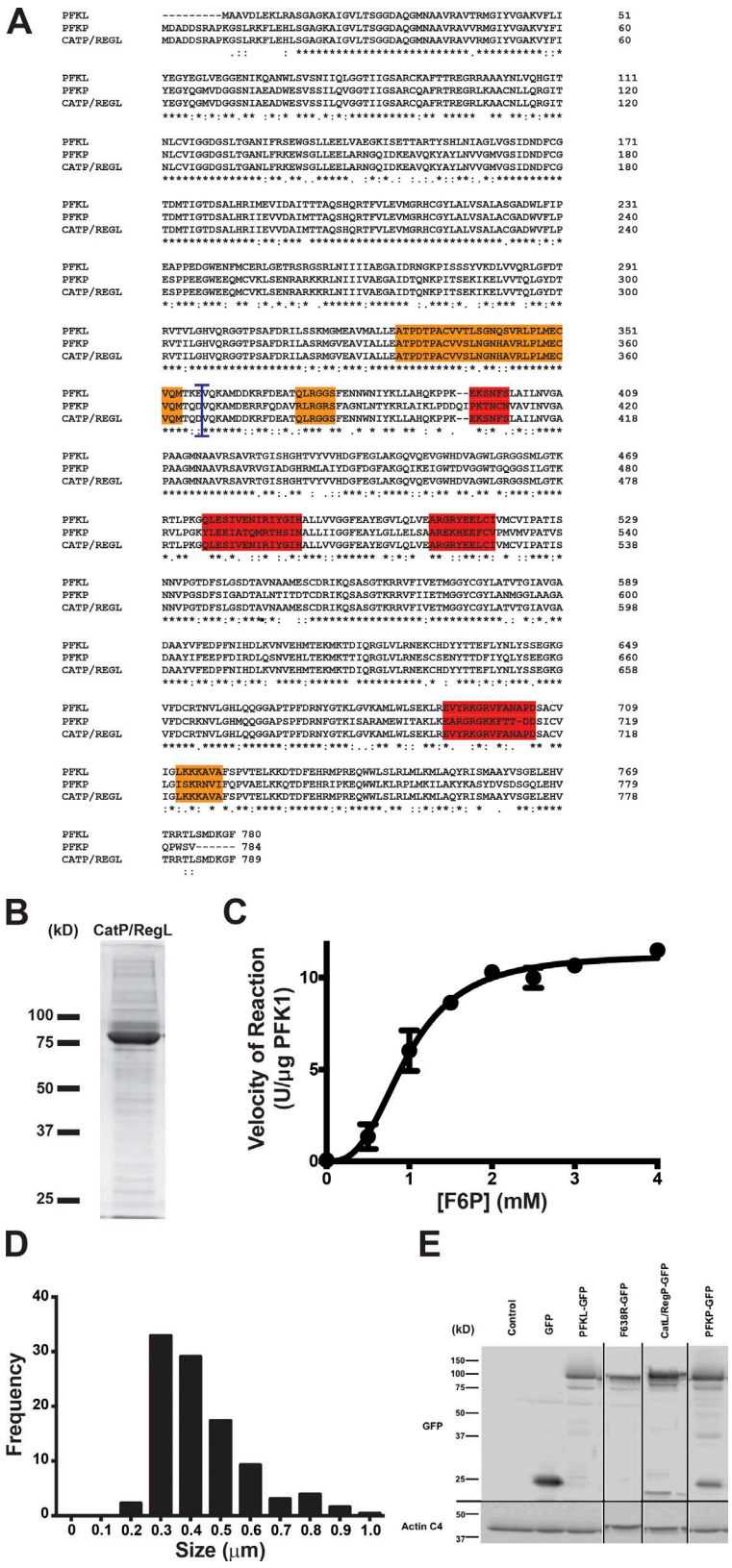

Figure S3. **Sequence, purification, and activity of CatP/RegL, size distribution of CIP, and immunoblot of PFK1-EGFP constructs.** (A) Sequence alignment of PFKL, PFKP, and CatP/RegL. Red and orange highlights correspond with interfaces 1 and 2, respectively. The blue bracket shows the area of fusion between the domains. Asterisks indicate fully conserved residues; colons indicate strongly conserved residues; and periods indicate weakly conserved residues. (B) Coomassie-stained SDS-PAGE of purified CatP/RegL. (C) Allosteric regulation of CatP/RegL by F6P. F6P affinity was performed at pH 7.4 with 0.1 mM ATP and 5 mM ammonium sulfate. Data are means ± SD of three determinations from two separate protein preparations. (D) Binned histogram of the size distribution, in µm, of citrate-induced PFKL-EGFP punctae (n = 258 particles from 24 cells from three independent preparations of cells). Frequency was measured as the percentage of particles in a given bin. (E) Immunoblot of EGFP and actin from lysates of 293^{FT} cells transiently expressing EGFP or PFK1-EGFP.

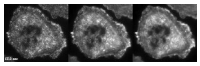

Video 1. **PFKL-EGFP forms dynamic particles with punctate localization in cells.** TIRF imaging of PFKL-EGFP–expressing MTLn3 rat mammary adenocarcinoma cells from a time-lapse sequence acquired at 10 frames per second (left image), and 1-s (10 frames; middle image) and 5-s (50 frames; right image) rolling averages highlighting docked PFKL-EGFP particles. The video corresponds with Fig. 4 (A–D).

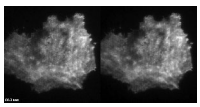

Video 2. **PFKP-EGFP is diffuse in cells.** TIRF imaging of PFKP-EGFP–expressing MTLn3 rat mammary adenocarcinoma cells from a time-lapse sequence acquired at 1.5 frames per second (left image), and 5-s (eight frames; right image) rolling average. The video corresponds with Fig. 4 E.

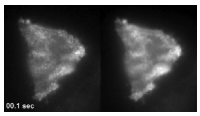

Video 3. **CatP/RegL-EGFP forms dynamic particles with punctate localization in cells.** TIRF imaging of CatP/RegL-EGFP–expressing MTLn3 rat mammary adenocarcinoma cell from a time-lapse sequence acquired at three frames per second (left image), and 5-s (15 frames; right image) rolling average highlighting docked particles. The video corresponds with Fig. 4 E.

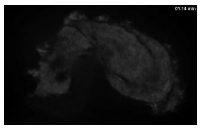

Video 4. **Citrate reversibly induces the formation of large PFKL-EGFP punctae.** Spinning-disk confocal image of PFKL-EGFP–expressing MTLn3 rat mammary adenocarcinoma cell from a time-lapse sequence acquired at two frames per minute. Cells were imaged in growth medium for 2 min before the addition of 10 mM citrate. After imaging for 5 min, the citrate-containing medium was replaced with growth medium, and cells were imaged for an additional 5 min. The video corresponds with Fig. 5 A.